

Mechanisms of Ti₃Al precipitation in hcp α -Ti

Felicity F. Dear^a, Paraskevas Kontis^b, Baptiste Gault^{b,a}, Jan Ilavsky^c, David Rugg^{a,d}, David Dye^a

^aDepartment of Materials, Royal School of Mines, Imperial College London, Prince Consort Road, London, SW7 2BP, UK

^bMax-Planck Institut für Eisenforschung GmbH, Max-Planck-Straße 1, Düsseldorf, Germany

^cArgonne National Laboratory, 9700 S. Cass Avenue, Building 433A, Argonne, IL 60439, USA

^dRolls-Royce plc, Elton Road, Derby, DE24 8BJ, UK

Abstract

Nucleation and growth of Ti₃Al α_2 ordered domains in α -Ti–Al–X alloys were characterised using a combination of transmission electron microscopy, atom probe tomography and small angle X-ray scattering. Model alloys based on Ti–7Al (wt.%) and containing O, V and Mo were aged at 550 °C for times up to 120 d and the resulting precipitate dispersions were observed at intermediate points. Precipitates grew to around 30 nm in size, with a volume fraction of 6–10% depending on tertiary solutes. Interstitial O was found to increase the equilibrium volume fraction of α_2 , while V and Mo showed relatively little influence. Addition of any of the solutes in this study, but most prominently Mo, was found to increase nucleation density and decrease precipitate size and possibly coarsening rate. Coarsening can be described by the Lifshitz-Slyozov-Wagner model, suggesting a matrix diffusion-controlled coarsening mechanism (rather than control by interfacial coherency). Solutionising temperature was found to affect nucleation number density with an activation energy of $E_f = 1.5 \pm 0.4$ eV, supporting the hypothesis that vacancy concentration affects α_2 nucleation. The observation that all solutes increase nucleation number density is also consistent with a vacancy-controlled nucleation mechanism.

Keywords: Titanium alloys, Phase transformations, Transmission electron microscopy (TEM), Atom probe tomography (APT)

1. Introduction

Predicting the lifetime of safety-critical components in gas turbine engines is crucial to continued improvements in flight safety. Despite a global increase of 90% in passenger journeys and 40% in freight transport by air in the decade to 2018 [1], the accident rate across the same time period dropped by 30% [2]. Sustaining this safety improvement relies on mechanistic understanding of the materials serving in such applications, and this same knowledge can steer the development of more capable alloys.

Titanium alloys form a key materials system for aerospace applications, with $\alpha+\beta$ alloys such as Ti–64 (Ti–6Al–4V, wt.%) widely used in fan and compressor components [3]. Deeper understanding of these alloys' response to fatigue loading has been an area of intense effort for several years [4, 5].

In $\alpha+\beta$ alloys, the elastic anisotropy and limited slip system availability of the hcp α phase have a significant impact on the polycrystalline material's overall response to static and cyclic loading regimes [6]. This means that, during high cycle or dwell fatigue loading, variations in elastic and plastic behaviour from grain to grain can initiate yielding near the boundary of particularly mismatched grains.

The nature of this intragranular plasticity plays a key role in fatigue crack initiation. If easy cross-slip is possible, dislocations are able to travel across an individual grain to intersect its grain boundaries at any location. If dislocations are instead restricted in their ability to cross-slip and travel homogeneously, slip bands are formed and eventually intersect a grain boundary. This results either in slip transmission, where the next grain in

its path is well oriented for deformation, or in a dislocation pile-up [7]. A sufficiently large pile-up may impose enough stress to nucleate a fatigue crack [8]. Groups of similarly-oriented grains (macrozones) and slip bands extending across millimetres have been implicated in dwell fatigue [9, 4, 10], including in service issues [11]. Slip band formation and factors promoting the even distribution of slip across the α microstructure are hence of significant interest.

Aluminium is commonly included at around 6 wt.% in $\alpha+\beta$ alloys, stabilising the α phase and providing solid solution strengthening. Phase segregation produces an α composition closer to 7 wt.% (11.8 at.%) meaning that, at temperatures of 500–700 °C, crystallographic ordering of Al can occur and lead to precipitation of the α_2 phase (Ti₃Al, DO₁₉ structure) [12]. The position of the $\alpha/\alpha+\alpha_2$ boundary has been the subject of several studies, with successive iterations of the Ti–Al phase diagram shifting it towards lower Al content [13, 14]. A region of short-range ordering (SRO) between truly disordered α and the $\alpha+\alpha_2$ field has also been proposed [15]. Recent diagrams place the boundary at around 10 at.% in calculated diagrams and 12 at.% in Schuster and Palm's diagram drawing together numerous experimental observations [16, 17, 18].

Even in the early stages of α_2 formation, where some form of ordering (evidenced by faint superlattice reflections) exists prior to precipitates being resolvable in dark field TEM images, there is a significant impact on slip behaviour [19]. Cross-slip is hindered, such that first dislocations passing across a grain disrupt the local ordering, leaving a trail of disrupted structure that offers an easier route for subsequent dislocations. This results in slip band formation and the associated deleteri-

ous micromechanical effects, with notable implications for tensile and fatigue response [5]. The earliest stages of ordered domain formation have been shown to restrict primary creep in α -Ti [20, 19]. Dislocation pinning by α_2 precipitates has also been observed [21]. In macroscopic plastic deformation, α_2 causes initial strain hardening followed by localised strain softening [19, 22], due to initial resistance to slip by the ordered domains being overtaken by the establishment of slip bands as easy paths for slip.

Studies on the formation mechanism of α_2 are challenging due to the nanometre length scales and small compositional variations between matrix and precipitate that are involved, especially during the early stages of phase separation. Long-term ageing at temperatures around 500–600 °C typically produces precipitates 5–10 nm in size. Morphology is spheroidal, with elongation along the shared c -axis occurring as growth proceeds and the precipitates undergo coarsening [23]. The earliest stages of phase separation remain less well understood. Possible mechanisms include homogeneous nucleation or spinodal decomposition, and a spinodal decomposition triggered by SRO has also been suggested [23, 24, 25].

The influence of additional alloying elements on α_2 formation is a significant consideration in trying to gauge the propensity of commercial alloys to deleterious Al ordering. Interstitial oxygen content has been shown to promote α_2 formation, shifting the $\alpha/\alpha+\alpha_2$ phase boundary to lower Al content and higher temperature [18, 26, 27, 28, 29]. This is suggested to be caused by a reduction in the solubility of Al in Ti with increasing O content [27]. The presence of β stabilisers in $\alpha+\beta$ alloys is also thought to influence α_2 formation [30].

This work investigates the factors controlling α_2 formation in an isothermal ageing study of a model alloy series based on Ti–7Al (wt.%), with additions of O, V and Mo. Microstructures were observed in TEM, and local compositions were measured in atom probe tomography. Precipitate dispersion parameters such as number density were analysed using small angle X-ray scattering. Insights are then drawn regarding the role of vacancies in nucleation, a hypothesis which is then tested, allowing the role of solutes in enhancing α_2 precipitation to be understood.

2. Experimental methodology

Alloys listed in Table 1 were melted from Ti sponge (Toho, Japan), TiO powder and pure Al, V and Mo pellet in an Arcast200 27 kW low pressure argon arc melter and cast to produce 23×23×55 mm ingots. The alloys were then rolled and recrystallised in the α phase followed by ice water quenching. Samples of each alloy in this IWQ (disordered) condition were taken, and 10 mm cubes were then encapsulated under an Ar atmosphere in quartz and aged at 550 °C for up to 120 d and furnace cooled, to evolve the α_2 precipitate dispersions. Separately, samples of each material from the quenched condition were subjected to 2 hours ageing at 550 °C before air cooling (AC condition), to capture the early stages of ordering.

Microstructures were initially observed in backscatter electron imaging on a Zeiss Sigma 300 FEG-SEM operated at 8 kV.

SEM specimens were prepared by electropolishing with a 3% perchloric acid solution at –35 °C and 20 V. Bulk compositions were confirmed using ICP-OES and combustion analysis provided by TIMET UK Ltd, Table 1.

Formation of α_2 was observed with conventional TEM methods, with specimens prepared by jet electropolishing with a 3% perchloric acid solution at –35 °C and 20 V to perforation. Using a JEOL 2100F TEM operated at 200 kV, selected area electron diffraction patterns were collected for each sample along $\langle 01\bar{1}1 \rangle$ directions. Dark field images of the α_2 precipitates were then made using the $\{2\bar{1}\bar{1}0\}_{\alpha_2}$ reflections. This provided qualitative observation of precipitate and dispersion characteristics, and allowed measurement of precipitate aspect ratios by measuring several wholly contained, clearly visible precipitates in images for each sample.

Measurement of compositional features of the precipitates at sub-nanometre resolution was performed using atom probe tomography (APT). Specimens were prepared by conventional Ga⁺ FIB lift-out methods [31]. Specific grain orientations were targeted using EBSD mapping prior to FIB work. This produced specimens with the APT analysis direction oriented within a few degrees of the $\langle 2\bar{1}\bar{1}0 \rangle$ zone axis. Titanium and Ti-based alloys are prone to forming hydrides during specimen preparation for TEM and APT, an artefact that can be avoided by performing the final thinning or sharpening of specimens at cryogenic temperatures [32]. Here, we used the infrastructure described in [33, 34] for cryogenic preparation, yet upon comparing with specimens obtained on the same FIB at room temperature, no significant differences in the H uptake were noticed. The low solubility of H in α -Ti and the targeted preparation far from any interfaces likely explains these observations. APT samples were then run on a Cameca LEAP 5000 XS operated in voltage mode at 50 K, with a pulse frequency of 200–250 kHz, pulse fraction of 20% and detection rate of 0.20–0.40%. The data collected were then analysed using Cameca’s IVAS analysis suite for reconstruction and MATLAB scripts for further analysis.

Quantification of dispersion statistics and precipitate evolution was achieved using small angle X-ray scattering (SAXS). Specimens were prepared by electrodischarge machining of a 3 mm diameter cylinder, from which discs of 300 μ m thickness were cut with a precision saw. The discs were then ground to the appropriate thickness (\sim 100 μ m) by hand using SiC grit papers up to a 4000 grit finish, followed by polishing with a neutralised colloidal silica solution by hand. After thorough cleaning with detergent to remove colloidal silica and isopropanol to remove surface contaminants, specimens were suspended in an amorphous, transparent tape for handling during measurement. SAXS measurements were then taken on the USAXS beamline [35] at the Advanced Photon Source at Argonne National Laboratory, using a 21 keV beam and a 800×800 μ m beam area. The data were reduced using the Nika package [36] and analysed using the Irena package [37] within Igor Pro. Morphological information from TEM imaging and compositional information from APT were used to guide the fitting of SAXS data with known shapes, aspect ratios and phase compositions, allowing deconvolution of volume fraction and contrast.

Table 1: Compositions of the Ti-7Al model alloy series measured by ICP-OES and combustion analysis by TIMET (Witton, UK). The hydrogen content in each alloy was measured to be 0.01 wt.% or less. Alloys in this study are referred to by their nominal compositions. Rolling (T_{roll}) and recrystallisation (T_{RX}) temperatures for these steps were chosen according to the β transus for each alloy, identified by iterative heat treatments and metallography. Recrystallisation times (t_{RX}) were chosen to account for the varying recrystallisation kinetics in each system.

Alloy (nominal composition)	Measured composition / wt.%					Measured composition / at.%					T_{roll} / °C	T_{RX} / °C	t_{RX} / h
	Al	V	Mo	O	N	Al	V	Mo	O	N			
Ti-7Al	6.58	<0.01	<0.01	0.05	0.02	11.09	<0.01	<0.01	0.14	0.06	900	980	1
-0.25O	7.14	<0.01	<0.01	0.24	0.05	11.95	<0.01	<0.01	0.68	0.16	900	980	1
-1.1V	7.01	1.21	<0.01	0.07	0.04	11.79	1.08	<0.01	0.20	0.13	900	850	1
-1.1V-0.25O	7.04	1.17	<0.01	0.26	0.08	11.80	1.04	<0.01	0.73	0.26	900	850	1
-0.8Mo	7.17	<0.01	0.83	0.10	0.08	12.08	<0.01	0.39	0.28	0.26	850	850	18
-0.8Mo-0.25O	7.16	<0.01	0.90	0.30	0.01	12.01	<0.01	0.42	0.85	0.03	850	850	18

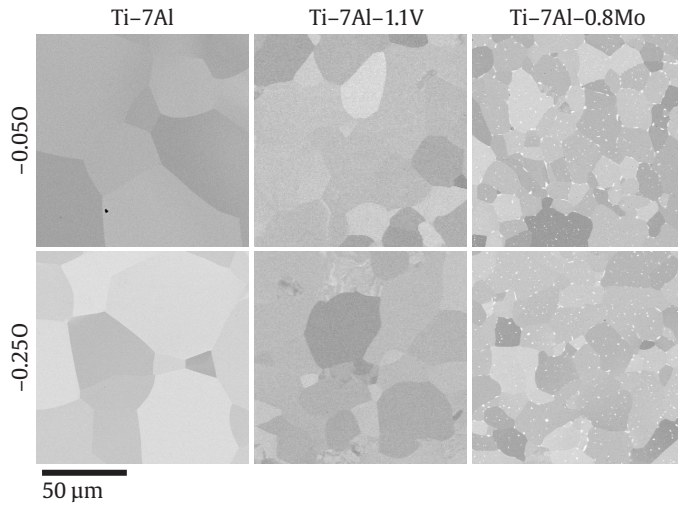


Figure 1: Backscatter micrographs of alloy microstructures, showing the intended equiaxed α microstructure. In the Mo-containing alloys, the very limited solubility of Mo in α led to the formation of small, micron-scale β domains at grain boundary triple points, which also contributed to grain size refinement during processing.

3. Results

3.1. Microstructural characterisation

Equiaxed α microstructures were produced, Fig. 1, with grain sizes of 10–50 μm depending on alloy composition. Alloys containing no β stabilisers showed a larger grain size due to the limited opportunity to restrict grain size during processing of material with a very narrow $\alpha+\beta$ phase field. The Mo-containing alloys contained a small fraction of β due to the very low solubility for Mo in α ; it was later demonstrated in APT results that the α phase contained a small amount of Mo, as intended.

3.2. Transmission electron microscopy

Selected area electron diffraction patterns taken for $\mathbf{B} = \langle 01\bar{1}1 \rangle$, Fig. 2, show the development of superlattice reflections as the ordered α_2 phase forms and grows. After a short hold of 2 hours at 550 °C, a small amount of intensity was observable at superlattice spot locations. Upon further ageing for 10 days or more, superlattice reflections became distinct spots and increased in intensity as ageing progressed.

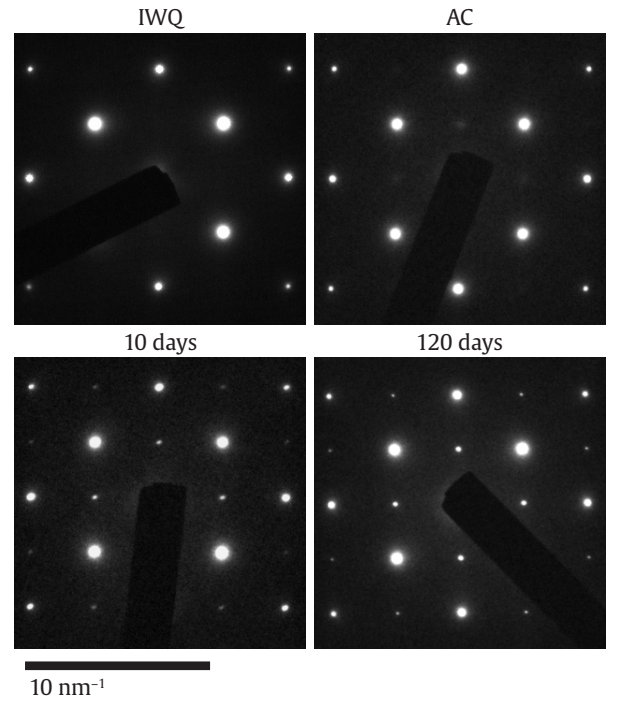


Figure 2: Selected area electron diffraction patterns ($\mathbf{B} = \langle 01\bar{1}1 \rangle$) obtained for Ti-7Al-0.05O (wt.%), in the ice water quenched (disordered) state, and in selected subsequent ageing states. Diffuse superlattice reflections are faintly visible after 2 hours ageing at 550 °C (AC condition), which intensify as phase separation progresses at 10 days and 120 days.

Dark field images provide a qualitative view of trends in precipitate morphology, size and number density during ageing, Fig. 3. Imaging was attempted for the 2 hour aged specimens, but no image contrast was evident. The base alloy Ti-7Al-0.05O showed formation of nanoscale precipitates after 10 days, which coarsened over time whilst growing in size and increasing in aspect ratio.

The addition of oxygen to the alloy system causes an increase in precipitate number density, and produces smaller precipitates. The effect of oxygen on volume fraction of the α_2 phase is unclear from qualitative micrographs; it should be recalled that these are projections of contrast through the foil thickness. TEM images do not show evidence of a significant effect of vanadium on the precipitate dispersion. The addition of molybdenum considerably restricts precipitate sizes, and precipitate

aspect ratio does not increase as significantly over the duration of the study. However, these micrographs only provide a qualitative impression of the alloying trends; for a quantitative comparison we turn next to atom probe tomography and SAXS.

3.3. Atom probe tomography

Atom probe tomography results provided a quantitative analysis of local compositional features. Of specific interest were the compositions of phases present, segregation of solutes between these phases, compositional features of the α/α_2 interface, and the crystallographic site partitioning of V and Mo on the α_2 DO₁₉ lattice. Measurements were performed for Ti-7Al-0.05O in the quenched condition as a reference dataset, for this alloy aged for 49 days, and for this alloy and Ti-7Al-0.25O, Ti-7Al-1.1V-0.25O and Ti-7Al-0.8Mo-0.25O in the 120-day aged condition to observe α_2 precipitates.

Data reconstruction was informed by TEM observations of precipitate morphology and by crystallographic information about the material. Since specimens were prepared from a known crystallographic orientation, partial indexing of desorption maps was possible and confirmed that the pole approximately parallel to the analysis direction was $\langle 2\bar{1}\bar{1}0 \rangle$ in each specimen. This allowed calibration of reconstruction parameters by guiding the reconstruction according to the known interplanar spacing of $\{2\bar{1}\bar{1}0\}$ planes in α -Ti.

Analysis of Ti-7Al-0.05O in the quenched condition revealed a homogeneous distribution of all solutes in species density maps, with no indications of phase separation. It is noted that the presence of short-range ordering versus true disorder cannot necessarily be inferred from APT data due to sub-100% ion detection efficiency. Upon ageing to 49 days, a dispersion of α_2 was evident in the specimen as regions of increased Al content, displaying the ellipsoidal morphology observed in TEM, Fig. 4. After 120 days at 550 °C, this alloy displayed the expected coarsening of precipitates. APT observations of alloys containing O, V and Mo additions showed precipitate dispersions with characteristics as expected from earlier TEM observations, with increased number density upon adding these solutes and reduced precipitate size in the Mo-containing alloys.

Proximity histograms (composition profiles calculated as a function of the distance to a specific isosurface [38]) were produced to analyse the nature and extent of phase segregation for each solute, Fig. 5. The α_2 phase was identified according to its Al enrichment to around 25 at.%.

Elements seen to promote α_2 formation in dark field TEM observations were expected to show segregation to this phase. For both O and V, segregation to the α matrix was instead observed. Previously we have shown [29] that O enhances α_2 formation whilst segregating to the α phase, owing the curvature of the phase boundary in the Ti-Al-O ternary system. Mo showed no segregation between the phases despite its significant effect on the α_2 precipitate dispersions.

For each specimen, proximity histograms were used to choose values for a set of Al concentration isosurfaces at 6.5% to select α and 10.5% to select α_2 without including the interfacial region. This approach was used to obtain phase com-

positions, Table 2. These phase compositions were used to provide contrast values for SAXS analysis, allowing deconvolution of the volume fraction and compositional contributions to peak size in the SAXS data.

The analysed α compositions appear low in Ti (or, equivalently, high in Al) compared to the bulk ICP-OES analysis (Table 1). This is a direct and unavoidable consequence of the large difference in evaporation field between Ti and Al, causing Ti to be preferentially under-counted due to multiple evaporation events [39, 40]. This bias is more pronounced in the α phase, and it should thus be noted that this could cause a slight underestimate (on the order of a few per cent) of SAXS contrast and hence a slight overestimate of the volume fractions presented in the below analysis of SAXS data. This consideration was incorporated in estimates of uncertainty for the dispersion characteristics calculated from the SAXS data.

Table 2: Bulk and phase compositions measured in APT (no background correction applied). Bulk compositions were analysed counting all ions in a dataset. For phase compositions, proximity histograms were used to determine values for a set of aluminium isoconcentration surfaces to isolate each phase, excluding the interfacial region.

Material	Ageing state		Composition / at.%					
			Ti	Al	O	V	Mo	N
Ti-7Al	IWQ	Bulk	84.0	14.4	0.8			0.7
		49 d	Bulk	83.3	15.2	0.8		
	120 d	α	84.2	14.2	0.9			0.7
		α_2	74.6	24.6	0.3			0.7
		Bulk	82.9	15.4	1.0			0.7
		α	83.3	14.8	1.1			0.7
-0.25O	120 d	α_2	74.1	24.7	0.4			0.8
		Bulk	81.8	16.4	1.1			0.7
	120 d	α	83.7	14.4	1.3			0.6
		α_2	72.7	25.7	0.9			0.6
-1.1V-0.25O	120 d	Bulk	82.2	15.2	1.0	1.2		0.4
		α	83.6	13.7	1.1	1.3		0.4
		α_2	72.4	25.5	0.6	0.9		0.6
-0.8Mo-0.25O	120 d	Bulk	83.7	14.5	1.0		0.4	0.4
		α	85.2	12.9	1.1		0.4	0.4
		α_2	75.8	22.7	0.6		0.4	0.4

3.4. Small angle X-ray scattering

SAXS curves for each alloy in the ageing study, Fig. 6, showed evolution of a peak at high scattering vector (Q) over time, along with a low- Q peak that showed no systematic variation with the ageing process. These are ascribed to α_2 precipitation and to the presence of grain boundaries as large scatterers respectively. The α_2 peak is distinctly visible for larger precipitates, but for very fine dispersions as in the Mo-containing materials it is less easily discerned. For all alloys, a slight difference in curve shape at high Q between quenched and air-cooled states is seen.

The raw data were fitted using two scatterer populations for each of the main features. A prolate spheroidal model was used for α_2 precipitates, based on TEM images showing that precipitate aspect ratio increases with time. This shape is described with a shorter equatorial radius r_e and longer polar radius r_p , so

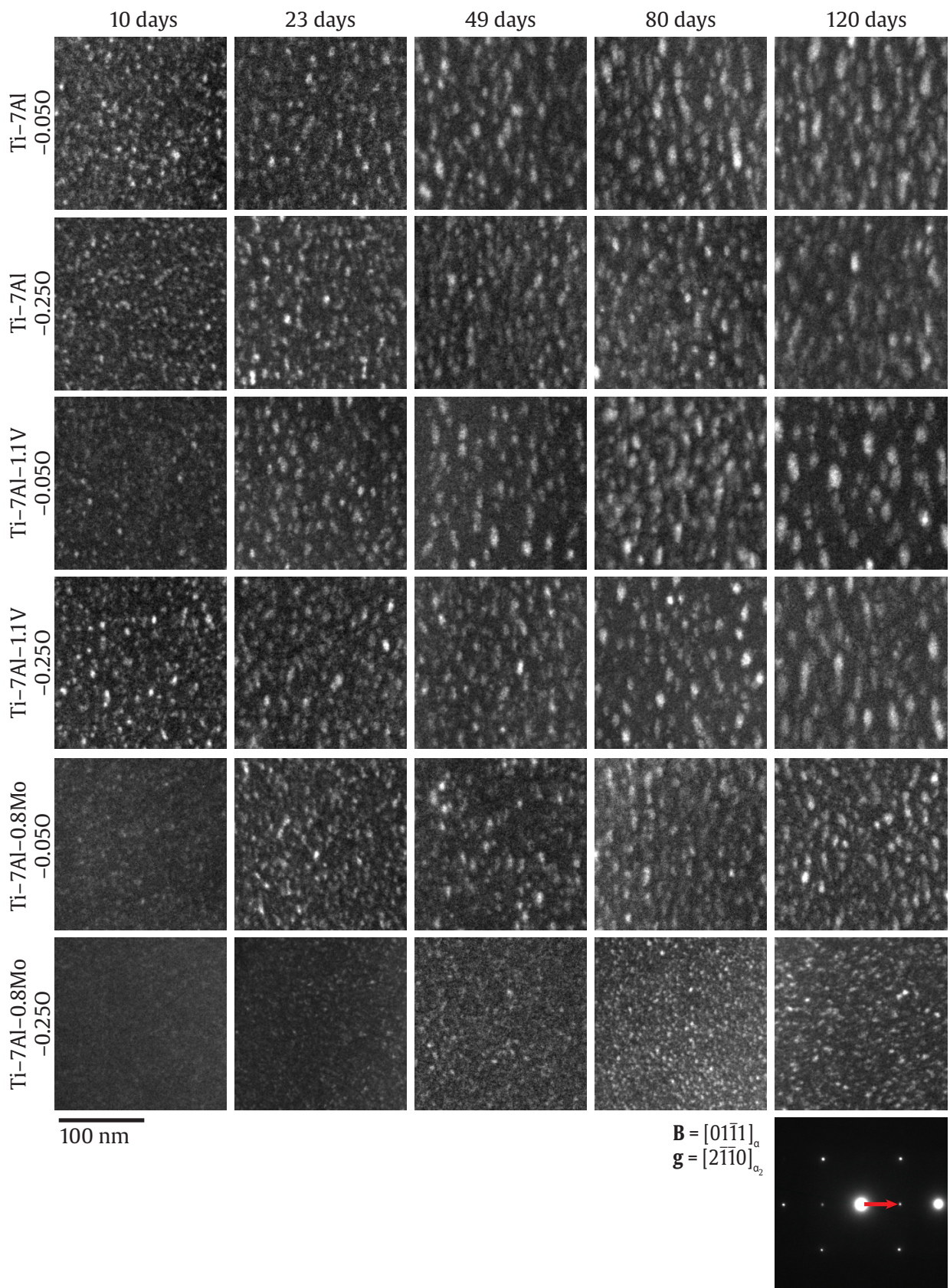


Figure 3: Dark field transmission electron micrographs recorded for specimens of each alloy at different ageing times, using a two-beam condition with the $[2\bar{1}\bar{1}0]$ reflection for $\mathbf{B} = [01\bar{1}1]$. The base alloy Ti-7Al-0.05O (wt.%) shows formation of spheroidal precipitates that increase in size and aspect ratio as ageing progresses. Additional solutes modify the way in which precipitate size, aspect ratio, spacing and number density evolve over time.

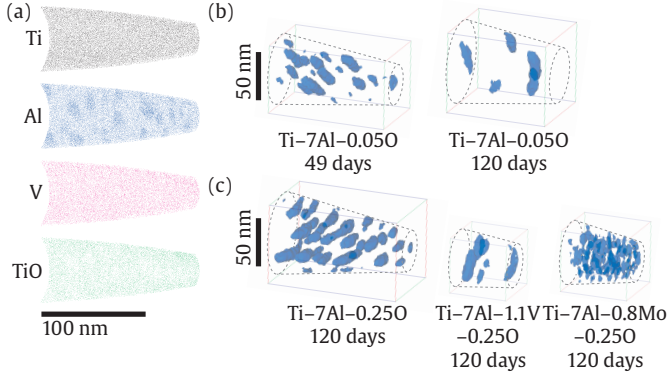


Figure 4: Examples of atom probe tomography results. (a) Atom maps showing the distribution of ion types detected for a specimen of Ti-7Al-1.1V-0.25O aged for 120 days at 550 °C. Note the domains of increased Al content, which are indicative of α_2 phase formation. O was detected only within TiO^{n+} complex ions. 8.5% Al concentration isosurfaces were used to indicate phase boundaries in aged specimens. The coarsening of α_2 precipitates is evident in comparing Ti-7Al-0.05O after ageing at 550 °C for 49 days and 120 days, (b). The precipitate dispersion characteristics seen in dark field TEM (Fig. 3) are reflected in the Al isosurfaces shown for different alloys after ageing for 120 days, (c).

that particle aspect ratio is given by $A = r_p/r_e$ and precipitate volume can be calculated as $V = \frac{4}{3}\pi r_e^3 A$. As seen in Fig. 6, a structure factor effect occurs in some of the samples (appearing as a dip in measured intensity at the low- Q shoulder of the α_2 peak). This effect is strengthened or subdued according to the competing effects of precipitate growth and coarsening on the extent to which each dispersion can be considered dilute.

Contrast values were calculated using the Irena analysis package [37], using composition data from APT. The α and α_2 compositions for each sample were used to calculate the average atomic weight of each phase. This was then used to estimate the density of the phase, assuming no difference in unit cell volume compared to pure Ti, and these phase compositions and densities were then used to calculate scattering length density contrast. After calculating this for the different samples, values between $1.7\text{--}2.7 \times 10^{20} \text{ cm}^{-4}$ were obtained but showed no systematic variation with alloy composition, so an average value of $2.2 \times 10^{20} \text{ cm}^{-4}$ was taken for fitting of all SAXS datasets in this study.

In the fitting process, A is an input parameter along with phase contrasts calculated in the Irena analysis suite using APT data. Model outputs include r_e and volume fraction of α_2 phase, f . These can be used to calculate precipitate number density, $n = f/v$, and if, in the absence of any specific model or description, a simple cubic array of precipitates in the matrix is assumed, the average spacing may be calculated as $s_{\text{eff}} = n^{-1/3}$. The low- Q peak associated with grain boundaries was modelled as a cylindrical disc of appropriate diameter and thickness, and fitted using an arbitrary contrast that was not deconvolved from volume fraction for this microstructural component.

Direct comparison of f between alloys is possible but, due to the variation in precipitate aspect ratio with both alloy and ageing time, the model output parameter r_e is not an appropriate metric for comparing precipitate sizes across the study. A

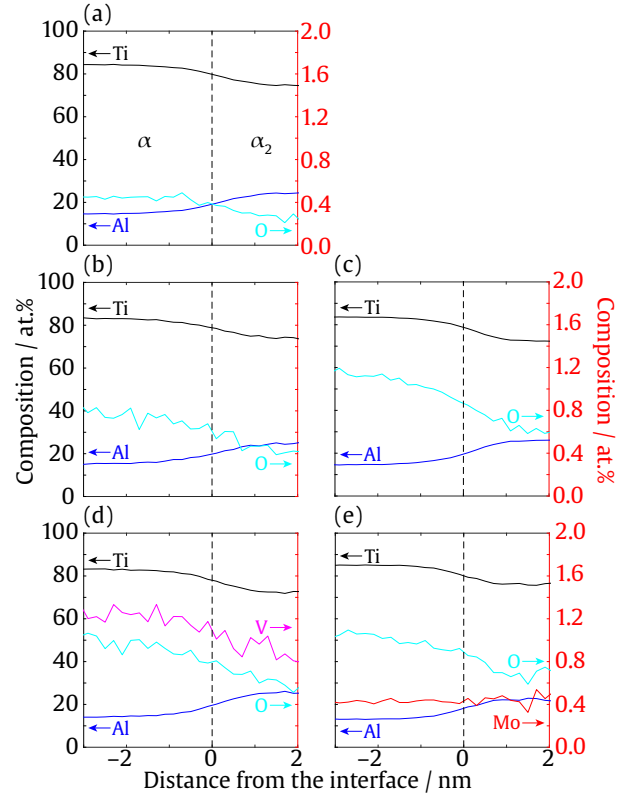


Figure 5: Proximity histograms constructed for the α/α_2 interface in APT datasets: (a) Ti-7Al-0.05O, aged 49 d; (b) Ti-7Al-0.05O, aged 120 d; (c) Ti-7Al-0.25O, aged 120 d; (d) Ti-7Al-1.1V-0.25O, aged 120 d; (e) Ti-7Al-0.8Mo-0.25O, aged 120 d. Segregation of aluminium to the α_2 at a concentration of approximately 25 at.% is evident, corresponding well with the expected Ti_3Al stoichiometry. Notably, oxygen is found to segregate to the matrix α phase in each alloy, despite the fact that it promotes α_2 formation. Vanadium shows a similar behaviour to oxygen, while molybdenum showed no clear segregation to either phase. (Ti, Al shown against black axis; O, V, Mo shown against red axis.)

directly comparable quantity is the average volume of a precipitate, $V = \frac{4}{3}\pi r_e^3 A$. For easy cross-reference with TEM images and APT reconstructions, the diameter of a sphere having equal volume to the modelled spheroid can be calculated as $d_{\text{eq}} = 2r_e A^{1/3}$. This equivalent sphere diameter provides a directly comparable metric of precipitate size at different ageing times, and allows easy comparison with TEM and APT data.

Fitting results for α_2 volume fraction, size and spacing showed similar trends with time for each alloy composition, but clear differences were apparent between different alloys, Fig. 7. Volume fraction f showed the expected rapid initial increase followed by plateauing towards the equilibrium volume fraction for each system. An equilibrium volume fraction was reached for the base alloy and variants containing additions of O, V or both. A higher fraction of α_2 was observed in Ti-7Al-0.25O compared to Ti-7Al. The addition of V alone caused no significant difference in volume fraction, and the addition of O to the V-containing alloys did not influence the fraction of α_2 . The Mo-containing alloys did not appear to reach an equilibrium state, with volume fraction still apparently increasing after 120 days at 550 °C. The final measured volume fractions for these

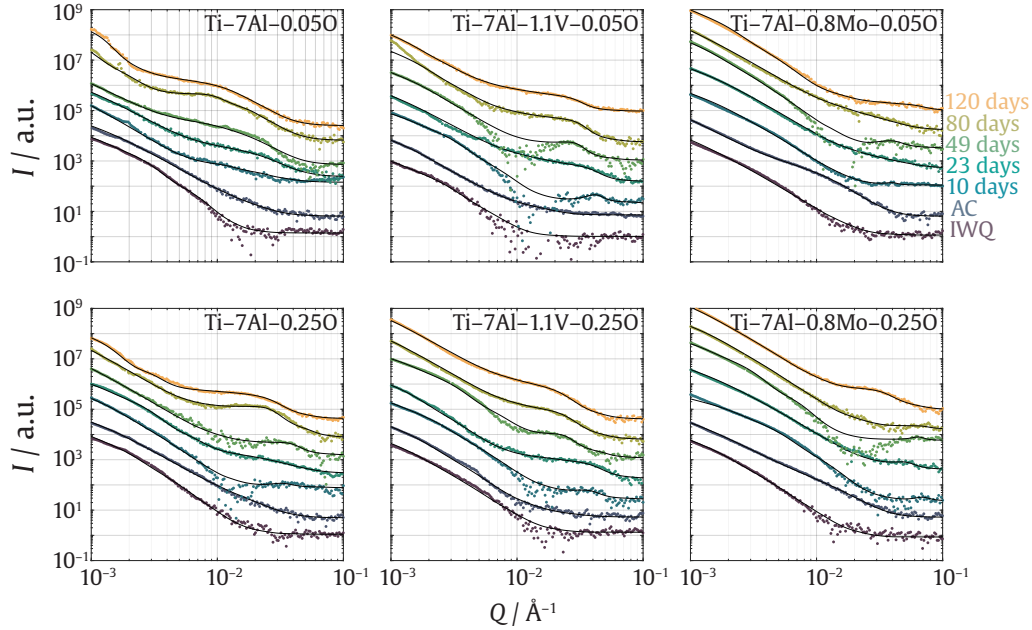


Figure 6: SAXS data obtained for the ageing study of the Ti–7Al model alloy series. In each case, a low- Q peak is present due to scattering from grain boundaries, and a peak at high Q develops with ageing time as the α_2 phase forms and grows. The variable influence of structure factor effects can be seen in different specimens, e.g. the Ti–7Al–1.1V–0.050 10-day sample, as a dip in intensity at the low- Q shoulder of the α_2 peak.

alloys after 120 days were slightly higher than for the base alloy. As with the V-containing alloys, no significant difference in volume fraction was seen between the Mo alloys with different O levels.

Precipitate size and spacing were reduced compared to the Ti–7Al base alloy upon adding any of the three solutes investigated. Mo had the most significant effect, producing very fine dispersions of small, closely-spaced precipitates. As with volume fraction, precipitate size and spacing showed no significant influence from oxygen content in the V- and Mo-containing materials. In each system, number density was found to vary as expected for precipitate coarsening behaviour, with an initial rapid increase corresponding to nucleation and early growth of precipitates. This was followed by a more gradual decrease as the microstructure underwent coarsening, with larger precipitates growing at the expense of smaller ones.

Comparing IWQ and AC datasets (i.e. quenched/disordered and SRO/early nucleation stage), a difference in curve shape is consistently seen across the different alloys. This takes the form of an increased intensity across a broad Q range from around 0.01 to 0.05 \AA^{-1} . Modelling of the AC datasets was attempted using a low aspect ratio spheroid, but produced unphysical modelling results.

3.5. APT crystallography

Attempts were made to analyse the APT data for crystallographic information, specifically regarding site partitioning of substitutional solutes V and Mo on the α_2 lattice. Spatial distribution maps (SDMs) were calculated for individual precipitates that had been identified as being located directly on a $\{2\bar{1}\bar{1}0\}$ pole, for Ti–Ti, Ti–Al and Ti–V species pairs, Fig. 8. However,

due to the significant differences in evaporation field between Ti and Al under the measurement conditions applicable to these alloys, artefacts were seen in the interplanar spacing both in atom maps and in SDMs. This artefact has been described by Vurpillot *et al.* [41]. By comparison, in Ni–Al γ – γ' alloys, the evaporation field difference is smaller so that site partitioning is more easily accessible through on-zone APT [42]. The low solubility of V and Mo in the α and α_2 phases also made this analysis challenging due to limited V or Mo atoms available for measurement and SDM analysis.

4. Discussion

The use of TEM, APT and SAXS in combination has allowed the analysis of volume fraction, size and spacing of α_2 in this set of model alloys. Comparisons between the various alloying elements may be made.

4.1. Volume fractions

First, considering volume fraction, the increase from 6% to 10% due to increased oxygen content supports the small shift in the position of the $\alpha/\alpha+\alpha_2$ boundary upon adding oxygen that has been previously suggested [27, 26, 28]. Based on the results of this study, vanadium does not appear to significantly alter the volume fraction of α_2 produced after 120 days ageing at $550 \text{ }^\circ\text{C}$. Molybdenum causes a slight increase from 6% to 8%, but due to retardation of phase separation kinetics by this solute, the Mo-containing systems did not reach equilibrium volume fractions during the 120 days of this study.

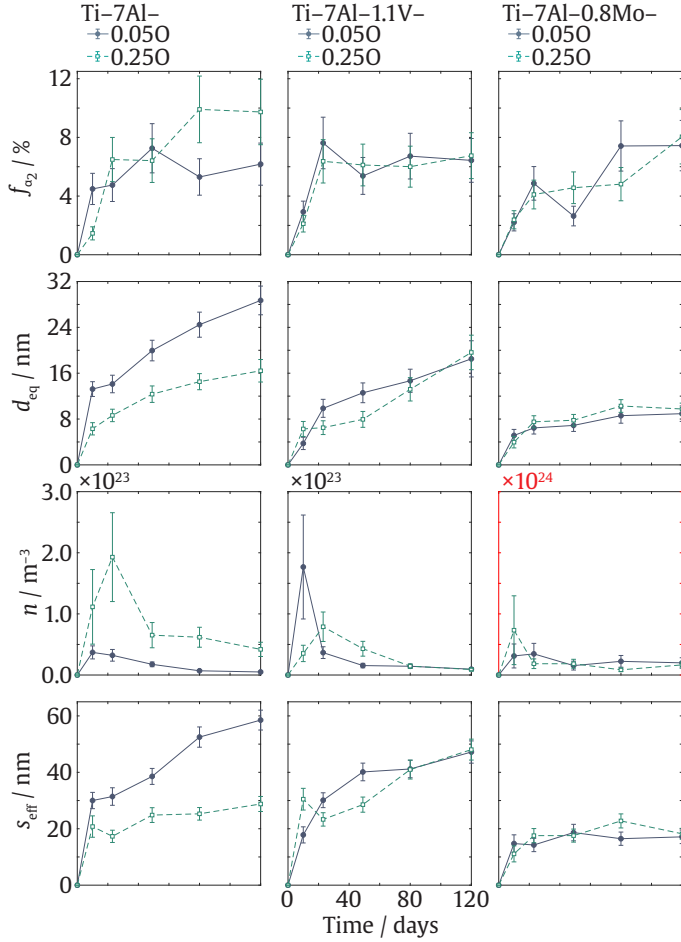


Figure 7: SAXS-derived quantitative analysis of the evolution of volume fraction f_{α_2} , precipitate equivalent diameter d_{eq} , number density n and effective square spacing s_{eff} . N.B. the 10 \times change in scale for the number density in the Mo-containing samples (shown with red axes); this solute has the most significant effect on n .

4.2. Size and spacing

Regarding the size and spacing of precipitates, these were largest at all times for the base alloy Ti-7Al-0.05O. Additions of any of the three solutes investigated caused refinement of the α_2 dispersion. Molybdenum had the most significant effect on this, followed by oxygen, while vanadium had a fairly minimal effect on the size and spacing of precipitates. The varying degrees of refinement are reflected in the extent to which each sample's scattering curve shows structure factor effects. Considering also the number density at short and long times for the different alloys, all solutes are seen to increase n during the early stages of phase separation. This suggests that adding any of these solutes causes increased nucleation density. Molybdenum produces an order of magnitude increase in early number density compared to the other alloys in the study. It is suggested that the resulting reduction in interparticle distances then causes smaller precipitate sizes due to soft impingement.

In the V- and Mo-containing alloys, there is little difference in volume fraction, size and spacing of α_2 precipitates between the low- and high-oxygen variants in each case. This indicates that the $\alpha/\alpha+\alpha_2$ boundary in the Ti-Al-O-V and Ti-Al-O-

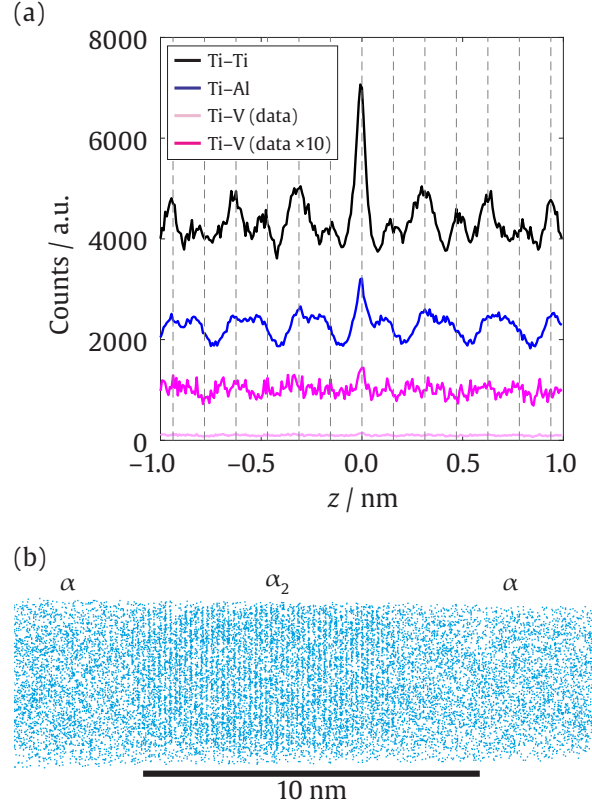


Figure 8: Crystallographic analysis was attempted for on-zone APT datasets containing ordered α_2 Ti₃Al precipitates, shown here for Ti-7Al-1.1V-0.25O (wt.%). For samples analysed parallel to a $\langle 2\bar{1}\bar{1}0 \rangle$ direction, α_2 precipitates lying on a crystallographic pole in the reconstruction were analysed to produce spatial distribution maps, (a). An artefact previously described by Vurpillot *et al.* [41] was seen in the interplanar spacings analysed for this dataset in both the spatial distribution maps (a) and the Al atom maps (b).

Mo quaternary systems becomes less sensitive to O as the β stabiliser content increases.

4.3. Coarsening and LSW modelling

In order to compare the precipitate growth rate and coarsening between alloys, the Lifshitz-Slyozov-Wagner (LSW) model was applied for the precipitate effective radius, $r = d_{eq}/2$ (for direct comparison between samples with different precipitate aspect ratios). This model describes the evolution of precipitate size with time according to

$$r^3(t) - r_0^3 = \frac{8\Gamma DCV_m^2}{9RT} t = K_{LSW} t,$$

where Γ is the precipitate/matrix interfacial energy, $D = D_0 \exp(-Q/RT)$ is the diffusion coefficient of the rate-limiting species through the matrix, C is the equilibrium concentration of the rate-limiting species in the matrix, V_m is the molar volume of the precipitate phase, R is the ideal gas constant and T is the absolute temperature at which phase separation has been observed [43, 44]. The gradients of linear fits hence provide a rate constant, K_{LSW} , that can be compared between alloys. There may be overlap between the growth and coarsening regimes for the α_2 dispersions observed, Fig. 7; in the first few days

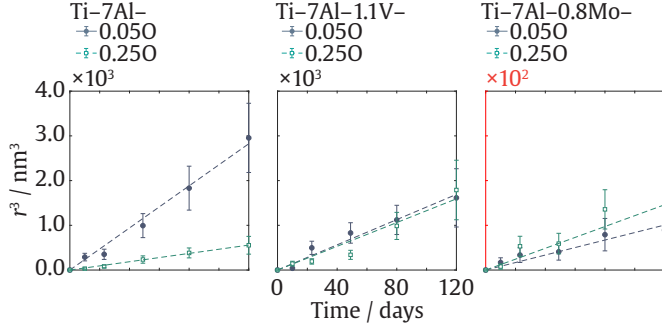


Figure 9: Lifshitz-Slyozov-Wagner modelling assumes that a precipitation coarsening process is controlled by the diffusion of a rate-limiting species through the matrix, leading to a linear proportionality between precipitate volume and time. Plotting r^3 against time, good linear fits were obtained for each alloy in the study, supporting a matrix diffusion-controlled coarsening mechanism for α_2 in α -Ti-Al.

Table 3: Lifshitz-Slyozov-Wagner modelling was successfully applied to the SAXS data, Fig. 9, with least-squares goodness of fit R_{LS}^2 of 0.91 or better. This model provides coarsening rate constants K_{LSW} and an estimate of the coarsening rate of precipitates in each alloy in terms of volume per unit time. It is noted that, for these alloys, there is likely a significant overlap of the growth and coarsening regimes. The peak precipitate number density during the coarsening process, as analysed in SAXS, is shown for comparison.

Material	K_{LSW} / $10^{-31} \text{ m}^3 \text{ s}^{-1}$	R_{LS}^2	Coarsening rate / $\text{nm}^3 \text{ d}^{-1}$	Peak n / 10^{22} m^{-3}
Ti-7Al	1.7 ± 0.1	0.98	15 ± 1	3.7
-0.25O	0.46 ± 0.03	0.98	4.0 ± 0.3	19.3
-1.1V	0.83 ± 0.07	0.97	7.2 ± 0.6	7.9
-1.1V-0.25O	0.79 ± 0.07	0.96	6.8 ± 0.6	17.7
-0.8Mo	0.08 ± 0.01	0.96	0.68 ± 0.06	34.6
-0.8Mo-0.25O	0.13 ± 0.02	0.91	1.1 ± 0.2	73.3

and in the Mo-containing alloys the phase fraction increases with time. The LSW approach does not deconvolve these two processes, such that the extracted K_{LSW} are not pure coarsening rates, especially in the case of Mo, but also incorporate growth rate to an extent depending on the degree of overlap between growth and coarsening stages. Nonetheless, this analysis allows some comparison of the phase separation kinetics between alloys. It is interesting to note that in the Ti-7Al-0.25O and V-containing alloys, a fairly consistent coarsening rate of $4\text{--}7 \text{ nm}^3 \text{ d}^{-1}$ is obtained.

A nonzero value of r_0 would indicate an incubation period between the introduction of isothermal ageing conditions and the onset of precipitation. In this study, $r_0 = 0$ was set for LSW fitting as no incubation period is expected nor evident in the data. Least squares linear regression for each alloy gave goodness of fit R_{LS}^2 values of 0.9 or above for a $1/3$ power law, Fig. 9, indicating a diffusion-limited growth process, rather than an interface-controlled mechanism [45]. The K_{LSW} values obtained for these alloys, Table 3, are reasonable when compared to those reported in an analogous study of $\gamma\text{--}\gamma'$ Ni superalloys [46], considering the much slower formation of α_2 in Ti-Al alloys than of γ' in Ni-Al alloys.

Comparing the rates obtained for the different alloy compositions, Table 3, and considering that a matrix diffusion-

controlled growth mechanism is supported by the good fits obtained for the LSW model, it may be anticipated that the growth rate would depend only on the diffusivity of the key species, aluminium. Although Mo has been seen to slow phase separation kinetics for the $\alpha \rightarrow \beta$ transformation [47], in this instance the Mo concentration is very low and considered unlikely to have such a stark effect on number density through modification of Al diffusivity alone. It is suggested instead that, due to soft impingement of solute fields around growing α_2 precipitates, the coarsening rate is controlled by the nucleation density of the precipitate dispersion, reflected by a correspondence between rate and interprecipitate spacing s_{eff} .

A further outcome of this study is that a value for the α/α_2 interfacial energy may be calculated, since this is a term contained in the rate constant K_{LSW} . Using the values given in Table 4, a value of $\Gamma = 107 \text{ mJ m}^{-2}$ was obtained for the base alloy Ti-7Al-0.05O. Since coarsening of Ti_3Al in Ti has not been quantified before, literature estimates for comparison are not available. It should be noted that the value inferred for Γ depends strongly on that assumed for D , which is itself an extrapolation from literature measurements at higher temperatures, and may be strongly affected by e.g. vacancy and minor solute content in the samples studied. For a factor of 10 change to the coarsening rate, if assumed to be entirely driven by Γ , this would imply an order of magnitude difference in the size of Γ between the alloys in this series, since the relationship is linear. This is unlikely given only minor differences in composition between alloys; a more sophisticated coarsening and growth analysis would be required to fully deconvolve the effects for the Mo-containing alloys, rather than the simplest possible dilute coarsening LSW analysis performed here.

Table 4: Parameters used in the calculation to estimate α/α_2 interfacial energy based on LSW fitting for the Ti-7Al-0.05O alloy. The equilibrium concentration C_{Al} corresponds to the 14.8 at.% Al measured for the α phase of this alloy after 120 d ageing at 550°C . $D_{\text{Al}}(550^\circ\text{C})$ and V_{m} are calculated using data from [48].

K_{LSW} / $10^{-31} \text{ m}^3 \text{ s}^{-1}$	$D_{\text{Al}}(550^\circ\text{C})$ / $\text{m}^2 \text{ s}^{-1}$	C_{Al} / mol m^{-3}	V_{m} / $\text{m}^3 \text{ mol}^{-1}$
1.7	6×10^{-24}	12.1×10^3	10.7×10^{-6}

4.4. Effect of quenching temperature on α_2 formation

A second heat treatment study was conducted in order to establish a clearer mechanistic connection between the tertiary solutes (O, V, Mo) and differences in α_2 formation. Upon adding any of the three solutes, refinement of the α_2 dispersion was observed, to a greater or lesser extent depending on the solutes included. Noting the homogeneous distribution of α_2 precipitates across α grains in these alloys, it was suggested that the nucleation points must correspond to a homogeneously distributed lattice defect. A plausible candidate is the vacancy concentration in each alloy. It was proposed that, upon adding any solute, the resulting increased entropy of the alloy causes an increase in vacancy concentration, and that this is the common underlying mechanism controlling nucleation density.

To establish whether a link exists between vacancy concentration and α_2 nucleation density, a single alloy composition was used, Ti-7Al-0.05O, while the thermal history of the samples prior to α_2 ageing was varied. Vacancy concentration in metals is known to have an empirically Arrhenius-type dependence on temperature. Aiming to control the vacancy concentration in samples prior to ageing, pieces of the alloy in the IWQ starting condition were annealed at 750 °C and 950 °C to generate two different vacancy concentrations while remaining within the α phase field and staying above α_2 formation temperatures. The samples were then ice water quenched, cleaned to remove any oxide, and encapsulated under argon in a quartz ampoule before ageing at 550 °C for 23 days. The resulting α_2 dispersions were then characterised using dark field TEM imaging and SAXS measurements Fig. 10. The SAXS data were fitted using a spheroidal precipitate shape with an aspect ratio of 2.0 and a contrast value of $2.2 \times 10^{-20} \text{ cm}^{-4}$, following the same methodology as for the main SAXS dataset.

In order to establish whether these results are consistent with a vacancy-controlled nucleation mechanism, the number densities in each sample were compared to predicted vacancy concentration behaviour. The vacancy concentration at a temperature T is empirically given by

$$N = N_0 e^{-E_f/k_B T},$$

where N_0 is a constant prefactor and E_f is the vacancy formation energy. For two different temperatures, T_1 and T_2 ,

$$\frac{N_1}{N_2} = \frac{\exp(-E_f/k_B T_1)}{\exp(-E_f/k_B T_2)},$$

such that

$$E_f = k_B \left(\frac{1}{T_2} - \frac{1}{T_1} \right)^{-1} \ln \left(\frac{N_1}{N_2} \right).$$

If it is assumed that $n \propto N_0$ independent of temperature, then the α_2 number densities n may be used to estimate the vacancy formation energy in Ti-7Al-0.05O.

For the samples quenched from 750 °C and 950 °C, number densities of $2.2 \times 10^{21} \text{ m}^{-3}$ and $3.5 \times 10^{22} \text{ m}^{-3}$ were obtained from SAXS data fitting respectively, Table 5. This gives an estimate of $E_f = 1.5 \pm 0.4 \text{ eV}$. Previous experimental studies for vacancy formation in α -Ti are relatively scarce, but comparison may be made with the findings of Hashimoto *et al.* [49] who measured a value of $1.27 \pm 0.05 \text{ eV}$ using positron annihilation. First-principles calculations for E_f in α -Ti have found values of 1.87 eV [50] and 1.97 eV [51]. The value obtained in the present work is consistent with these earlier studies, lending support to a vacancy-mediated nucleation mechanism for α_2 in α -Ti-Al-X alloys, as a second-order effect of tertiary solute additions.

5. Conclusions

In this study, the precipitation and coarsening of α_2 Ti₃Al in a Ti-Al alloy series was studied, using TEM to identify the existence of the precipitates and their morphology, APT to characterise their composition, and SAXS to quantify their number

Table 5: SAXS fitting results for specimens solutionised at and quenched from different solutionising temperatures, T_{sol} , prior to ageing for 23 days at 550 °C in order to compare the effects of different vacancy concentrations on volume fraction f_{α_2} , precipitate size as equivalent sphere diameter d_{eq} and precipitate number density n . For both materials, a contrast value of $2.2 \times 10^{20} \text{ cm}^{-4}$ and an aspect ratio of 2.0 were used.

$T_{sol} / \text{°C}$	f_{α_2}	d_{eq} / nm	$n / 10^{21} \text{ m}^{-3}$
750	0.012	21.8	2.21
950	0.058	14.7	34.9

density, size and fraction. The effect of interstitial solute O and substitutional solute V and Mo, and of quenching temperature, were examined. The following conclusions are drawn.

- Interstitial O increases the volume fraction of α_2 formed at equilibrium, which is in the region of 8-10 vol%, while V and Mo have a relatively small effect. The precipitates grow in size to up to 30 nm after 120 d at 550 °C (Ti-7Al-0.05O), with interparticle spacing of a similar magnitude;
- Addition of O, V or Mo increases the nucleation density of α_2 , and leads to a finer precipitate dispersion;
- Growth of α_2 can be described using an LSW model, indicating diffusion control (rather than interface coherency

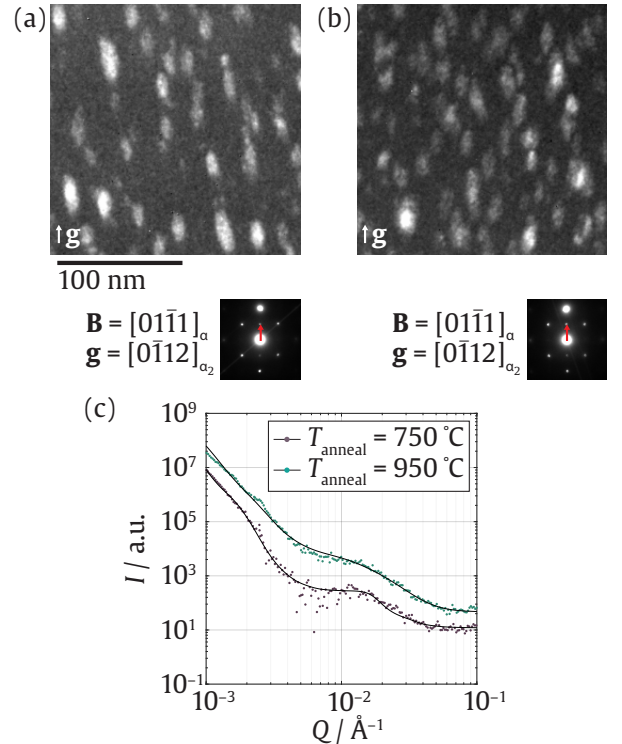


Figure 10: Effect of quenching temperature on α_2 formation, where Ti-7Al-0.05O specimens were aged for 23 days after quenching from annealing temperatures T_{anneal} (a) 750 °C and (b) 950 °C, freezing in lower and higher vacancy concentrations prior to ageing respectively. Dark field TEM shows the expected spheroidal morphology and a qualitative indication of different dispersion characteristics. SAXS measurements of these samples showed clear differences in the position and intensity of the α_2 peak, as well as the influence of structure factor (associated with higher number density) for the 950 °C sample.

control);

- A secondary study comparing α_2 formation between samples differing only by quenching temperature showed a difference in nucleation number density. This gave an activation energy consistent with a vacancy nucleation mechanism, $E_f = 1.5 \pm 0.4$ eV;
- This leads to the inference that the effect of solute O, V and Mo is, broadly, to increase the nucleation number density and thereby slow coarsening due to an earlier onset of soft impingement.

Acknowledgements

FFD was funded by Rolls-Royce plc and by the EPSRC Centre for Doctoral Training in the Advanced Characterisation of Materials (EP/L015277/1). DD was funded by a Royal Society Industrial Fellowship and EPSRC (EP/K034332/1). BG and PK are grateful for funding from the Max Planck Society through the Laplace project. The authors are grateful to U. Tezins, C. Bross and A. Sturm for their technical support of the APT and FIB facilities at the Max-Planck Institut für Eisenforschung, and for useful discussions with S. Balachandran. This research used resources of the Advanced Photon Source, a U.S. Department of Energy (DOE) Office of Science User Facility operated for the DOE Office of Science by Argonne National Laboratory under Contract No. DE-AC02-06CH11357. Useful conversations and technical assistance are also gratefully acknowledged from D. Isheim at Northwestern and A. Minor, R. Zhang and R. Traylor at UC Berkeley and Lawrence Berkeley National Laboratory, along with the help of K.M. Rahman and I. Bantounas at Imperial with the alloy processing.

References

- [1] World Bank Data, 2020. Air transport, passengers carried (IS.AIR.PSGR) and Air transport, freight (million ton-km) (IS.AIR.GOOD.MT.K1) [retrieved 20 September 2020].
- [2] International Civil Aviation Organization, 2020. Accident Statistics [retrieved 20 September 2020].
- [3] R. R. Boyer, An overview on the use of titanium in the aerospace industry, *Materials Science and Engineering: A* 213 (1996) 103–114. International Symposium on Metallurgy and Technology of Titanium Alloys.
- [4] W. J. Evans, M. R. Bache, Dwell-sensitive fatigue under biaxial loads in the near-alpha titanium alloy IMI685, *International Journal of Fatigue* 16 (1994) 443–452.
- [5] M. C. Brandes, M. J. Mills, J. C. Williams, The influence of slip character on the creep and fatigue fracture of an α Ti-Al alloy, *Materials Science and Engineering A: Structural Materials Properties Microstructure and Processing* 41 (2010) 3463–3472.
- [6] F. P. E. Dunne, D. Rugg, A. Walker, Lengthscale-dependent, elastically anisotropic, physically-based hcp crystal plasticity: application to cold-dwell fatigue in ti alloys, *International Journal of Plasticity* 23 (2007) 1061–1083.
- [7] S. Joseph, I. Bantounas, T. C. Lindley, D. Dye, Slip transfer and deformation structures resulting from the low cycle fatigue of near-alpha titanium alloy Ti-6242Si, *International Journal of Plasticity* 100 (2018) 90–103.
- [8] F. P. E. Dunne, D. Rugg, On the mechanisms of fatigue facet nucleation in titanium alloys, *Fatigue & Fracture of Engineering Materials & Structures* 31 (2008) 949–958.
- [9] M. J. Mills, S. Ghosh, S. Rokhlin, M. C. Brandes, A. L. Pilchak, J. C. Williams, The evaluation of cold dwell fatigue in Ti-6242, Federal Aviation Administration Report: DOT/FAA/TC-17/57 (2018).
- [10] D. F. Neal, Creep fatigue interactions in titanium alloys, *Proceedings of the Sixth World Conference on Titanium* (1988) 175–180.
- [11] Bureau d’Enquêtes et d’Analyses pour la Sécurité de l’Aviation Civile, Accident to the AIRBUS A380-861 registered F-HPJE and operated by Air France on 30/09/2017 en route over Greenland (report BEA2017-0568), 2020.
- [12] P. C. Gehlin, The crystallographic structure of Ti₃Al, 1970. *The Science, Technology and Application of Titanium*, ed. R.I. Jaffee and N.E. Promisel. Pergamon Press, New York, NY, USA.
- [13] T. K. G. Nambodhiri, C. J. McMahon, H. Herman, Decomposition of the α -phase in titanium-rich Ti–Al alloys, *Metallurgical Transactions* 4 (1973) 1323–1331.
- [14] S. Sircar, K. Narasimhan, K. Mukherjee, An investigation of the ordered DO₁₉ phase formation in the Ti–Al system, *Journal of Materials Science* 21 (1986) 4143–4146.
- [15] T. K. G. Nambodhiri, On the Ti–Al phase diagram, *Materials Science and Engineering* 57 (1983) 21–22.
- [16] V. T. Witusiewicz, A. A. Bondar, U. Hecht, S. Rex, T. Y. Velikanova, The Al–B–Nb–Ti system: III. Thermodynamic re-evaluation of the constituent binary system Al–Ti, *Journal of Alloys and Compounds* 465 (2008) 64–77.
- [17] H. Wang, R. C. Reed, J.-C. Gebelin, N. Warnken, On the modelling of the point defects in the ordered B2 phase of the Ti–Al system: Combining CALPHAD with first-principles calculations, *Calphad* 39 (2012) 21–26.
- [18] J. C. Schuster, M. Palm, Reassessment of the binary aluminum-titanium phase diagram, *Journal of Phase Equilibria and Diffusion* 27 (2006) 255–277.
- [19] T. Neeraj, M. J. Mills, Short-range order (SRO) and its effect on the primary creep behavior of a Ti–6wt.% Al alloy, *Materials Science and Engineering A: Structural Materials Properties Microstructure and Processing* 319 (2001) 415–419.
- [20] T. Neeraj, D.-H. Hou, G. S. Daehn, M. J. Mills, Phenomenological and microstructural analysis of room temperature creep in titanium alloys, *Acta Materialia* 48 (2000) 1225–1238.
- [21] J. C. Williams, A. W. Sommer, P. P. Tung, The influence of oxygen concentration on the internal stress and dislocation arrangements in α titanium, *Metall. Mater. Trans. B* 3 (1972) 2979–2984.
- [22] M. J. Blackburn, J. C. Williams, Metallurgical aspects of the stress corrosion cracking of titanium alloys, Proc. Conference on fundamental aspects of stress corrosion cracking. Houston, Texas, National Association of Corrosion Engineers (1969) 620–637.
- [23] M. J. Blackburn, The ordering transformation in titanium-aluminum alloys containing up to 25 at. pct aluminum, *Transactions of the Metallurgical Society of AIME* 239 (1967) 1200–1208.
- [24] H. Liew, G. D. W. Smith, A. Cerezo, D. J. Larson, Experimental studies of the phase separation mechanism in Ti-15at% Al, *Materials Science and Engineering A: Structural Materials Properties Microstructure and Processing* 270 (1999) 9–13.
- [25] H. Wood, G. D. W. Smith, A. Cerezo, Short range order and phase separation in Ti–Al alloys, *Materials Science and Engineering A: Structural Materials Properties Microstructure and Processing* 250 (1998) 83–87.
- [26] R. M. Waterstrat, Effect of Interstitial Elements on Phase Relationships in the Titanium–Aluminum System, 1988.
- [27] J. Y. Lim, C. J. McMahon, D. P. Pope, J. C. Williams, The effect of oxygen on the structure and mechanical behavior of aged Ti–8 wt pct Al, *Metallurgical and Materials Transactions A: Physical Metallurgy and Materials Science* 7 (1976) 139–144.
- [28] G. T. Gray, G. Lütjering, J. C. Williams, The influence of oxygen on the structure, fracture, and fatigue crack propagation behavior of Ti-8.6 wt. pct Al, *Metallurgical and Materials Transactions A: Physical Metallurgy and Materials Science* 21 (1990) 95–105.
- [29] P. A. J. Bagot, A. Radecka, A. P. Magyar, Y. Gong, D. C. Bell, G. D. W. Smith, M. P. Moody, D. Dye, D. Rugg, The effect of oxidation on the subsurface microstructure of a Ti-6Al-4V alloy, *Scripta Materialia* 148 (2018) 24–28.
- [30] A. Radecka, P. A. J. Bagot, T. L. Martin, J. Coakley, V. A. Vorontsov, M. P. Moody, H. Ishii, D. Rugg, D. Dye, The formation of ordered clusters in Ti–7Al and Ti–6Al–4V, *Acta Materialia* 112 (2016) 141–149.
- [31] K. Thompson, D. Lawrence, D. J. Larson, J. D. Olson, T. F. Kelly, B. Gorman, In situ site-specific specimen preparation for atom probe tomography, *Ultramicroscopy* 107 (2007) 131–139.
- [32] Y. Chang, W. Lu, J. Guénolé, L. T. Stephenson, A. Szczepaniak, P. Kontis, A. K. Ackerman, F. F. Dear, I. Mouton, X. Zhong, D. Raabe, B. Gault,

- S. Zhang, D. Dye, C. H. Liebscher, D. Ponge, S. Korte-Kerze, D. Raabe, B. Gault, Ti and its alloys as examples of cryogenic focused ion beam milling of environmentally-sensitive materials, *Nature Communications* 10 (2019) 942.
- [33] L. T. Stephenson, A. Szczepaniak, I. Mouton, K. A. K. Rusitzka, A. J. Breen, U. Tezins, A. Sturm, D. Vogel, Y. Chang, P. Kontis, A. Rosenthal, J. D. Shepard, U. Maier, T. F. Kelly, D. Raabe, B. Gault, The Laplace project: an integrated suite for correlative atom probe tomography and electron microscopy under cryogenic and UHV conditions, *PLOS One* 13 (2018) e0209211.
- [34] N. A. Rivas, A. Babayigit, B. Conings, T. Schwarz, A. Sturm, A. G. Manjón, O. Cojocar-Mirédin, B. Gault, F. U. Renner, Cryo-focused ion beam preparation of perovskite based solar cells for atom probe tomography, *PLoS ONE* 15 (2020).
- [35] J. Ilavsky, F. Zhang, R. N. Andrews, I. Kuzmenko, P. R. Jemian, L. E. Levine, A. J. Allen, Development of combined microstructure and structure characterization facility for *in situ* and *operando* studies at the Advanced Photon Source, *Journal of Applied Crystallography* 51 (2018) 867–882.
- [36] J. Ilavsky, *Nika*: software for two-dimensional data reduction, *Journal of Applied Crystallography* 45 (2012) 324–328.
- [37] J. Ilavsky, P. R. Jemian, *Irena*: tool suite for modeling and analysis of small-angle scattering, *Journal of Applied Crystallography* 42 (2009) 347–353.
- [38] O. C. Hellman, J. A. Vandenbroucke, J. Rüsing, D. Isheim, D. N. Seidman, Analysis of three-dimensional atom-probe data by the proximity histogram, *Microscopy and Microanalysis* 6 (2000) 437–444.
- [39] D. R. Kingham, The post-ionization of field evaporated ions: A theoretical explanation of multiple charge states, *Surface Science* 116 (1982) 273–301.
- [40] Z. Peng, F. Vurpillot, P.-P. Choi, Y. Li, D. Raabe, B. Gault, On the detection of multiple events in atom probe tomography, *Ultramicroscopy* 189 (2018) 54–60.
- [41] F. Vurpillot, A. Bostel, E. Cadel, D. Blavette, The spatial resolution of 3D atom probe in the investigation of single-phase materials, *Ultramicroscopy* 84 (2000) 213–224.
- [42] P. A. J. Bagot, O. B. W. Silk, J. O. Douglas, S. Pedrazzini, D. J. Crudden, T. L. Martin, M. C. Hardy, M. P. Moody, R. C. Reed, An Atom Probe Tomography study of site preference and partitioning in a nickel-based superalloy, *Acta Materialia* 125 (2017) 156–165.
- [43] I. M. Lifshitz, V. V. Slyozov, The kinetics of precipitation from supersaturated solid solutions, *Journal of Physics and Chemistry of Solids* 19 (1961) 35–50.
- [44] C. Wagner, Theorie der Alterung von Niederschlägen durch Umlösen, *Zeitschrift für Elektrochemie* 65 No. 7/8 (1961) 581–591.
- [45] A. J. Ardell, Trans-interface-diffusion-controlled coarsening in ternary alloys, *Acta Materialia* 61 (2013) 7749–7754.
- [46] V. A. Vorontsov, J. S. Barnard, K. M. Rahman, H.-Y. Yan, P. A. Midgley, D. Dye, Coarsening behaviour and interfacial structure of γ' precipitates in Co-Al-W based superalloys, *Acta Materialia* 120 (2016) 14–23.
- [47] A. K. Ackerman, A. J. Knowles, H. M. Gardner, A. A. N. Németh, I. Bantounas, A. Radecka, M. P. Moody, P. A. J. Bagot, R. C. Reed, D. Rugg, D. Dye, The kinetics of primary alpha plate growth in titanium alloys, *Metallurgical and Materials Transactions A* 51 (2020) 131–141.
- [48] G. Lütjering, J. C. Williams, *Titanium*, Springer Berlin Heidelberg, 2nd edition, 2007.
- [49] E. Hashimoto, E. A. Smirnov, T. Kino, Temperature dependence of the doppler-broadened lineshape of positron annihilation in α -Ti, *Journal of Physics F: Metal Physics* 14 (1984) L215–L217.
- [50] D. Connétable, J. Huez, É. Andrieu, C. Mijoule, First-principles study of diffusion and interactions of vacancies and hydrogen in hcp-titanium, *Journal of Physics: Condensed Matter* 23 (2011) 405401.
- [51] A. T. Raji, S. Scandolo, R. Mazzarello, S. Nsengiyumva, M. Härting, D. T. Britton, Ab initio pseudopotential study of vacancies and self-interstitials in hcp titanium, *Philosophical Magazine* 89 (2009) 1629–1645.